A&A manuscript no.
(will be inserted by hand later)

Your thesaurus codes are:
9(02.03.3; 06.01.3; 06.07.2; 06.15.1; 06.16.2)

ASTRONOMY AND ASTROPHYSICS

Small-scale topology of solar atmosphere dynamics

III. Granular persistence and photospheric wave amplitudes

N.M. Hoekzema[1,2], P.N. Brandt[2], and R.J. Rutten[1]

[1] Sterrekundig Instituut, Postbus 80000, NL–3508 TA Utrecht, The Netherlands
[2] Kiepenheuer-Institut für Sonnenphysik, Schöneckstr. 6, D–79104 Freiburg, Germany

Received; accepted

Abstract. We use a superb five-hour sequence of 900 solar images taken at La Palma to study long-duration persistence in the solar granulation, in the context of the long-lived "intergranular holes" discovered by Roudier et al. (1997) and the contention that these mark sites of convective downflow plumes. We develop a procedure to locate "persistency regions" that contain granular brightness maxima or minima over extended periods (up to 45 min), while allowing for lateral drifts due to horizontal flows. Statistical evaluation of the co-location probability for different pixel classes is first used to quantify the likelihood of long-term stationarity for different granular brightness classes and for the persistency regions, and then to evaluate the amount of preferential alignment, at different frequencies and time delays, between excessive Fourier modulation and granular brightness and persistence.

The results support the existence of long-lived intergranular holes. There is large persistency difference between the brightest and the darkest features; some of the latter have location memories as long as two hours. In addition, the darkest intergranular features are found to be sites of enhanced Fourier modulation in the 3-min acoustic regime, improving earlier results through much higher statistical significance. However, the persistency regions containing intergranular holes do not seem to produce the excess acoustic emission that would be expected above downflow plumes.

Key words: Sun: atmosphere – Sun: photosphere – Sun: granulation – Sun: oscillations – Convection

1. Introduction

This is the third paper in a series employing statistical methods to explore local relations between fine structure and wave amplitudes in the quiet solar atmosphere on the basis of image sequences obtained with the Swedish Vacuum Solar Telescope (SVST) on La Palma. The preceding papers (Hoekzema et al. 1998b, henceforth Paper I; Hoekzema et al. 1998a, henceforth Paper II) used data taken in 1990 to chart spatial alignments between granular morphology, chromospheric brightness patterning and spatial maps of short-duration temporal Fourier amplitude distributions in the photosphere and chromosphere. Paper I gave evidence for the occurrence of localized wave sources and wave diffraction near the solar surface, while various time-delay alignment charts constructed in Paper II suggest that the localized sources have mesoscale patterning and undergo mesoscale pattern migration.

The wider science context of our work was detailed in Paper I. The specific issues that we address here are the existence of long-lived features in the solar granulation and whether these are sites of enhanced photospheric wave amplitudes, taking up the discussion raised by Brown (1991), Brown et al. (1992), Goode et al. (1992), Restaino et al. (1993), Espagnet (1994), Rimmele et al. (1995), Espagnet et al. (1996) and Roudier et al. (1997). In particular, the last authors describe their finding of long-lived dark features, called "intergranular holes" by them, as a result of their search for vortex features similar to the large granulation whirlpool discovered by Brandt et al. (1988) which persisted for 79 min at one location. These intergranular holes consist of small dark sites in intergranular lanes that are continuously visible for over 45 min and appear to be preferentially located in mesoscale convergence centers. Roudier et al. (1997) suggest that the holes mark convective downflow plumes.

Such hole–plume identification is tempting in the light of other studies. Numerical modeling of the solar granulation suggests the existence of fast and rather stable downflows that funnel cool material deeply down into the convection zone ("plumes", "fingers", "vertically coherent structures", "chimneys"; e.g., Stein & Nordlund 1989; Cattaneo et al. 1991; Brummell et al. 1996) and are even regarded as major convective driving agent by Rast (1995) and Rieutord & Zahn (1997). In addition, kinematic and

Send offprint requests to: R.J. Rutten

dynamic magnetoconvection modeling indicates that magnetic fields gather preferentially in such strong downflows (e.g., Simon et al. 1991, 1995; cf. Spruit et al. 1991). Observational support comes from G-band imaging with very high spatial resolution, showing that the Muller network bright points marking "fluxtube" sites of strong magnetic field always reside in intergranular lanes (e.g., Muller et al. 1989; Muller & Roudier 1992; Roudier et al. 1994; Berger et al. 1995; Berger & Title 1996). If the picture of plume-driven magneto-convection holds and the intergranular holes mark plumes, it is likely that they possess enhanced vorticity because the convergent flows will tend to concentrate angular momentum into these locations (the "bath tub effect"). Roudier et al. (1997) suggest that small fluxtubes at these vortex sites may therefore be heated by their vorticity-induced footpoint twisting. However, direct observational validation of this process requires vorticity maps that resolve features considerably smaller than individual granules; such small-scale vorticity mapping is yet beyond the reach of current observational techniques.

The identification of the dark intergranular holes observed by Roudier et al. (1997) with convective downflow plumes is also not yet established, even if the title of their paper uses "plumes" instead of "holes" as if it were proven. We study this issue here by using the techniques of Paper I & II to search for these holes and to investigate whether they display the enhanced acoustic emission that downflow plumes are thought to generate. We take up pertinent hints in Papers I & II, in particular the suggestion of persistency of dark granulation features in Fig. 1 of Paper II in the form of a co-alignment tail that extends far beyond characteristic granule lifetimes and the statistically significant excess of waves of 2–4 min periodicity above dark intergranular lanes present in Fig. 5 of Paper I and Fig. 5 of Paper II.

The approach in this paper follows Papers I & II. We use similar reduction and measurement procedures (Sect. 2) and apply the same short-duration high-resolution Fourier analysis technique to produce wave amplitude maps for spatial correlation with the concurrent photospheric morphology. We again measure the amount of spatio-temporal alignment at varying time delays between different features through the statistical correspondence factor C that was introduced in Paper I. It is employed to quantify granulation persistency in Sect. 3.1 (Figs. 5 and 6) and to quantify co-alignment of excess wave amplitudes with granular morphology including persistency in Sect. 3.2 (Figs. 7 and 8).

The main improvement over Papers I & II is that a much better data set is used for the present analysis. The 1990 data were limited in field extent, so that the results in Papers I & II may suffer from selection effects and lack of statistics. Only a single full internetwork (supergranulation) cell and only a few mesogranulation cells were covered by the 1990 filtergrams. Since our approach in these papers is to employ extensive averaging over selected pixel classes in order to assess their statistical alignment probability, a technique that is dictated by the need to disentangle the highly complex mix of structures and wave modes present in the solar atmosphere (Paper I), it is important to increase the amount of data to improve the statistical significance. In addition, the 1990 data were taken under varying seeing conditions, resulting in good spatial resolution but not the superb quality reached at La Palma since. In this paper we perform similar analyses on a ten times larger data set that is also of much better quality, being part of the outstanding sequence of granulation images obtained by Simon et al. (1994). There is no accompanying image sequence of the overlying chromosphere, as was the case for the 1990 data used in Papers I & II, so that the present analysis is limited to photospheric topology. The next paper of this series will use the same material to study mesoscale patterning.

2. Data description and data analysis

2.1. Observations

The present analysis is based on a superb sequence of granulation images that was obtained on June 5, 1993 with the Swedish Vacuum Solar Telescope on La Palma (SVST, aperture 48 cm; see Scharmer & Lofdahl 1991; Scharmer 1989; Scharmer et al. 1985). The observing and initial reduction procedures have been described in detail by Simon et al. (1994) so that a short summary suffices here.

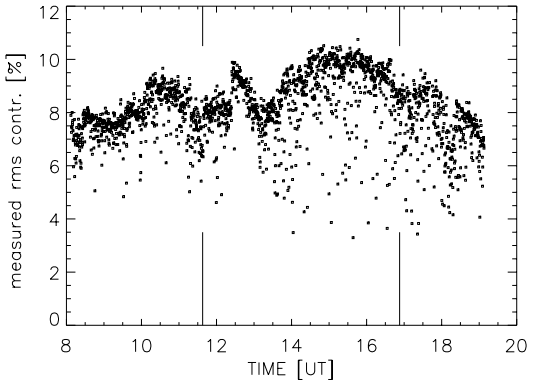

Fig. 1. Temporal variation of the measured rms intensity contrast per image. Excellent seeing corresponds to values around and above 8%. The vertical lines mark the segment analyzed in this paper

In its secondary focus, the telescope supplied a partial image of the solar disk through a 10 nm bandpass filter centered at a wavelength of 468 nm that was recorded by a Kodak Megaplus Model 1.4 CCD camera at a frame rate of 3.7 Hz. Each frame consisted of 1310 by 970 pixels with 8-bit digitization. A frame selection system (see Scharmer & Lofdahl 1991) determined the rms contrast

over a selected subfield in real time and selected the two best images out of the 55 frames taken per 15 s interval. Since the subsequent storage to magnetic tape took about 6 s, the total cycle time was close to 21 s. The image scale was 0.125 arcsec/pixel. Typical exposure times were 10–14 ms. The field of view was centered slightly south-east of the sunspot group NOAA 7519 which was situated at N05/E15 in the morning of June 5, 1993. The small follower spot of the group was kept centered on a four-quadrant cell via a servo tracking system. Due to the alt-azimuth construction of the telescope, the field of view rotated around this tracking spot.

Thanks to the excellent seeing conditions, an image sequence of outstanding quality and length was obtained. From 8:07 to 19:07 UT the rms intensity contrast of most frames ranged between 7 and 11% at a median value of 8.0%, as can be seen in Fig. 1. The present analysis uses the 900 frames covering the period 11:38–16:53 UT, a 5.25 h time span.

2.2. Reduction

All frames were corrected for the dark response of the CCD, flat-fielded by division through a defocused and motion-blurred image, derotated around the pivot point defined by the tracking spot and normalized to equal mean intensity to take out variations in exposure time and sky transparency. The next steps comprised the correction of full-field image shifts to better than 1 pixel, destretching (i.e., correction for subfield image distortions caused by atmospheric seeing, see Shine et al. 1994), and correction for the telescope diffraction pattern through applying a Wiener filter as described by Sobotka et al. (1993) and Hirzberger et al. (1997) with the signal-to-noise parameter set to 15. A subfield of 512 by 512 pixels was selected, avoiding the more active area that contained the tracker spot, and the 900 frames were interpolated onto equal time steps of 21.05 s. This made it possible to Fourier transform the data and apply a subsonic filter with a cutoff phase velocity of 4 km s^{-1} (e.g., Title et al. 1989) in order to remove oscillations and residual seeing distortions. Since the frames were apodized for this Fourier filtering, we finally selected an undisturbed subfield of 460×460 pixels, corresponding to 41.7×41.7 Mm^2. An example is shown in Fig. 2.

2.3. Intensity binning

The following procedure was employed to quantify granular morphology. First, each pixel was normalized by the local mean brightness obtained from averaging over the surrounding subfield of 19×19 pixels (1.7×1.7 Mm^2). This procedure serves to remove the larger-scale intensity fluctuations caused by the remaining solar five-minute oscillation as well as any seeing-induced brightness gradients. It is described in detail in Sect. 3 of Paper I.

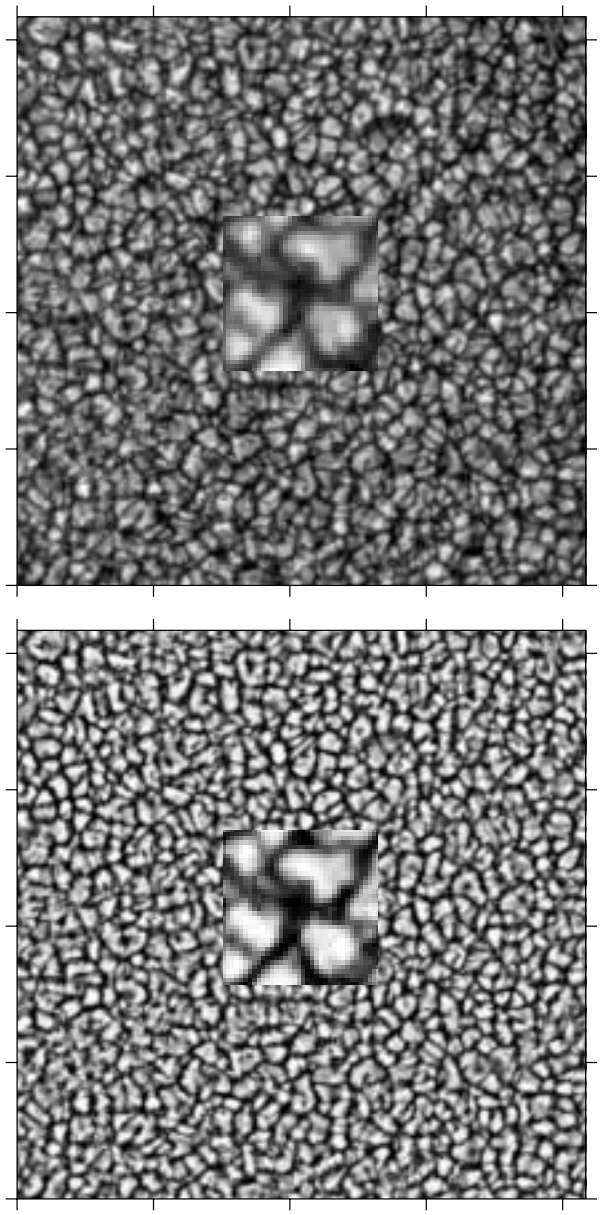

Fig. 2. Top: example image after destretching and subsonic filtering. Registration time 14:48:26 UT, rms intensity contrast 9.3%. Bottom: the same frame after local-area normalization and histogram equalization. Insets: enlargements of the central area. Scale: field size 41.7×41.7 Mm^2, ticks at 10 Mm intervals

All images were then histogram-equalized, i.e., the pixel brightnesses were rescaled such that equal contour intervals contain the same number of pixels. For example, the pixels with brightness 0–5% of the maximum value also cover 5% of the field in each normalized image. This is done in order to diminish the frame-to-frame contrast changes caused by variable seeing and to obtain compara-

ble statistics for different brightness categories. Figure 2 also shows the example subfield after this rescaling.

The range between minimum and maximum brightness per image was divided into 20 such contour bins, each covering one-twentieth of the field. The pixels in the lowest 5% bin nearly always belong to the very darkest parts of intergranular lanes, while those in the highest 5% bin are maxima within the brightest granules. The intermediate bins, in particular those in the range 40–55%, generally represent granular edges between granules and intergranular lanes.

2.4. Persistency binning

For the persistency analysis we aim at identifying granular features with lifetimes exceeding the characteristic granular evolutionary time scale of 5–15 min. Since horizontal flows in the photosphere may move features around at speeds of 0.5–1.0 km/s, as determined by Simon et al. (1994) from the same image sequence, we use a finding procedure in which brightness extrema are allowed to move around over small distances rather then requiring exact positional stability. It therefore differs intrinsically from the persistency-finding method of Roudier et al. (1997) who locate brightness minima in stacked sums of binarized images distinguishing granules from lanes in one-bit coding. They so find places that are persistently dark over long duration only when these maintain position exactly.

Our first step is to select all pixels in each frame that represent local maxima or minima and that also belong to the brightest or darkest 10% in the field. These pixels are used to define the centers of small subfields measuring 9×9 pixels (0.8×0.8 Mm). Our next step is to construct binary maps in which a pixel is assigned the value unity when it lies within such subfields in at least 36 out of 45 consecutive images, value zero otherwise. This procedure identifies small areas that contain one or more brightness extrema during 13–16 min. Such binary maps were constructed from overlapping 16-min image sequences that are spaced 5.25 min apart.

The resulting binary maps are then used to search for bright and dark features that exist even longer by locating pixels with value unity in seven consecutive maps, spanning a duration of about 45 min (6×5.25 min plus $36 \sim 45 \times 21$ s) which considerably exceeds the characteristic granular lifetime and equals the intergranular hole persistence measured by Roudier et al. (1997). In order to allow for small horizontal drifts, the fourth map in each sequence of seven maps was used directly while the unit-value areas containing brightness extrema were increasingly enlarged for the earlier and later maps in each sequence. Specifically, a 2-pixel (0.18 Mm) wide perimeter was added to the unit-value areas in maps 3 and 5 in each sequence, a 4-pixel perimeter in maps 2 and 6, and a 6-pixel perimeter in maps 1 and 7. This procedure limits the duration to about 45 min, since significant overlaps between unit-value regions begin to occur when more pixels are added.

Even with these spatial extensions there are only a few pixels with value unity in all seven binary maps per sequence. They cover 2.2% of the field when brightness minima are selected and only 0.7% when they contain brightness maxima. These filling factors are too low for reliable statistical analysis. Additional perimeter pixels surrounding the seven-map unit-value areas were therefore added to produce "persistency regions" with a total filling factor close to 5% so that they provide statistics comparable to the intensity bins in our correspondence plots below. Since there are three times as many locations with dark-feature persistency than with bright-feature persistency, the latter tend to grow to larger size from the addition.

The end result of this casting for persistent features consists of 44 binary "persistency maps" spaced at 5.25 min intervals over 3.7 h of the 5.25 h total duration (edge effects excluding the remainder). Their value-unity areas mark "persistency regions" with diameters of $0.4-1.0$ Mm, within which smaller bright or dark intensity extrema existed most of the time during about 45 minutes, even if they moved around somewhat.

Figure 3 shows examples of the actual locations of persistency regions by superimposing them on a sequence of partial image samples. The center panel is the fourth one in the sequence of seven binary maps defining these particular persistency regions over 45 min. The dark-minimum persistency regions are marked by white contours, the bright-maximum ones by dark contours. The sequence illustrates the extraordinary quality of the data set. There is no immediately obvious relationship between persistency and granular morphology, other than that persistency regions with dark minima contain dark lanes in the middle panel, those with bright maxima bright granules. Note that the latter do not mark network bright points in intergranular lanes. The apparent concentration in the right-hand part may reflect network patterning.

2.5. Fourier mapping

Three non-overlapping 22.4-min segments were selected from the image sequence, each containing 64 images. Following the procedure described in Paper I they were apodized to an effective duration of about 15 min to produce pixel-by-pixel Fourier amplitude maps at different periodicities. This duration is short enough to resolve granular pattern evolution, while long enough to discriminate between 5-min and 3-min wave modes. In order to diagnose the latter, we used the destretched data without applying a subsonic filter. Paper I explored the properties of such short-duration high-resolution Fourier maps in detail.

Figure 4 presents enlargements of a small part of the new maps from the 1993 data. They exhibit much fine

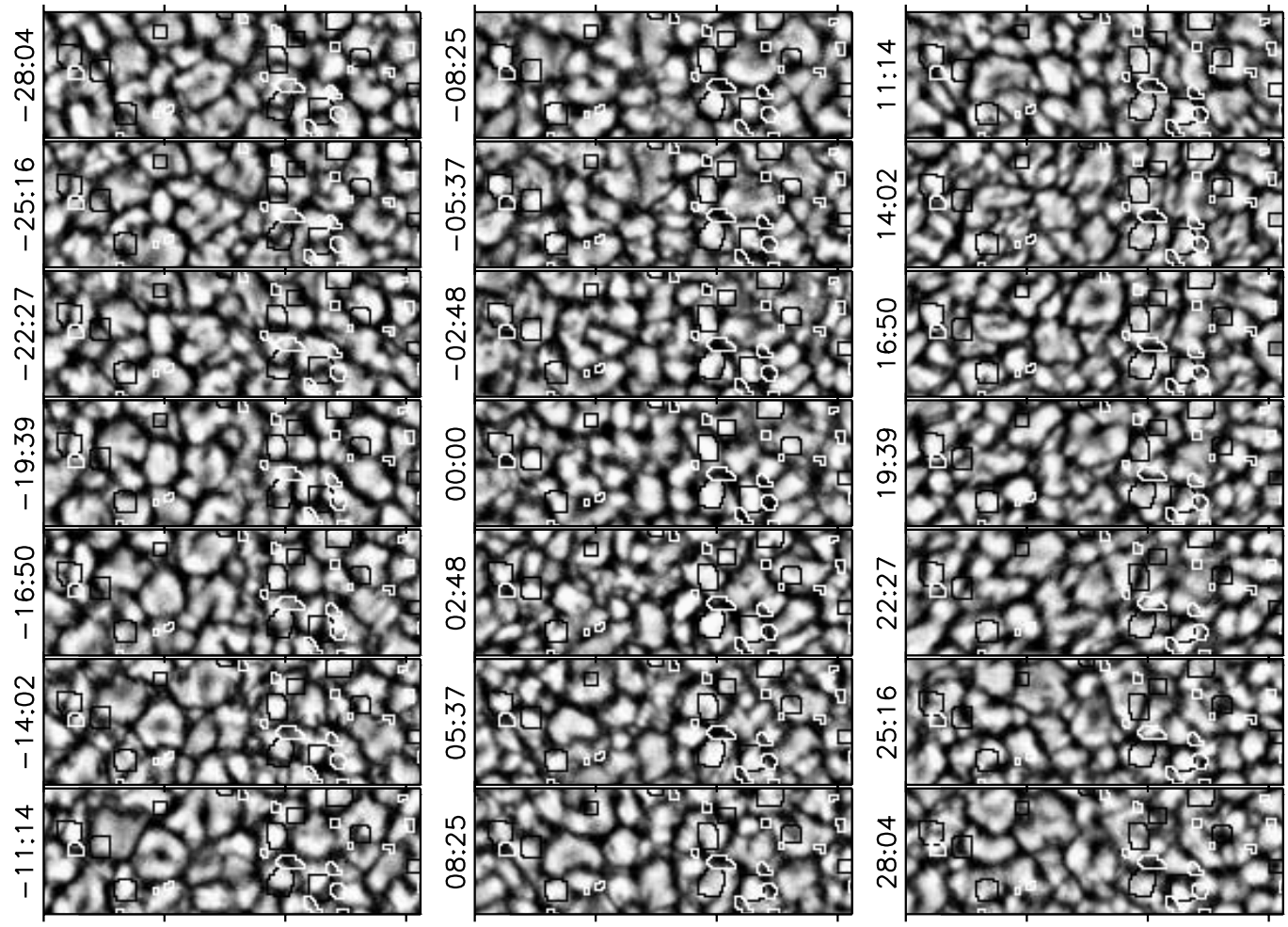

Fig. 3. Persistency regions overlaid on locally-normalized histogram-equalized partial images covering 56 min from top left to bottom right in 168.4 s steps. White contours: persistency regions containing dark minima. Black contours: persistency regions containing bright maxima. The panel at $\Delta t = 0$ (12:12:19 UT) corresponds to the central map of the persistency-finding procedure. Scale: 15.6×5.3 Mm^2 field, ticks at 5 Mm intervals. The lefthand column contains a fine example of an exploding granule at $x = 5$ Mm

structure with large amplitude contrast and with morphological difference between the generally roundish high amplitude regions and the slender, rope-like regions of low amplitude. This patterning is qualitatively the same as in the comparable logarithmic display in the lefthand column of Fig. 7 in Paper I, indicating that it is intrinsically solar and not due to the seeing which was much better during the 1993 observations. There is no distinct correspondence with the granular morphology in the bottom panel, which displays the zero-frequency pattern and represents an average of the destretched images over the effective 15-min measurement interval. Thus, the new maps confirm the results of Paper I where the morphological difference between high and low power patterning is attributed to inhomogeneous wave excitation and wave diffraction.

In the analyses below we concentrate on regions of large amplitude, i.e., those locations that have Fourier amplitudes over twice the map average. They cover 4–6% of the field, comparable to the intensity bins and the persistency regions.

2.6. Spatial correspondence

We again measure spatial alignments with a statistical tool called "spatial correspondence". It was introduced in Sect. 3 of Paper I and quantifies the cospatiality of two features or pixel classes between two different images or maps. It is defined as $C = f_{\rm AB}/f_{\rm B}$ where the coincidence filling factor $f_{\rm AB} = N_{\rm AB}/N_{\rm A}$ specifies the fraction of pixels of type A in one map that also belong to type B in another map and with the filling factor $f_{\rm B} = N_{\rm B}/N$ measuring the spatial occurrence of the second category. With this normalization C quantifies cospatiality in terms of the random-draw likelihood, $C = 1$ suggesting that A and B are independent phenomena while values $C > 1$ imply that

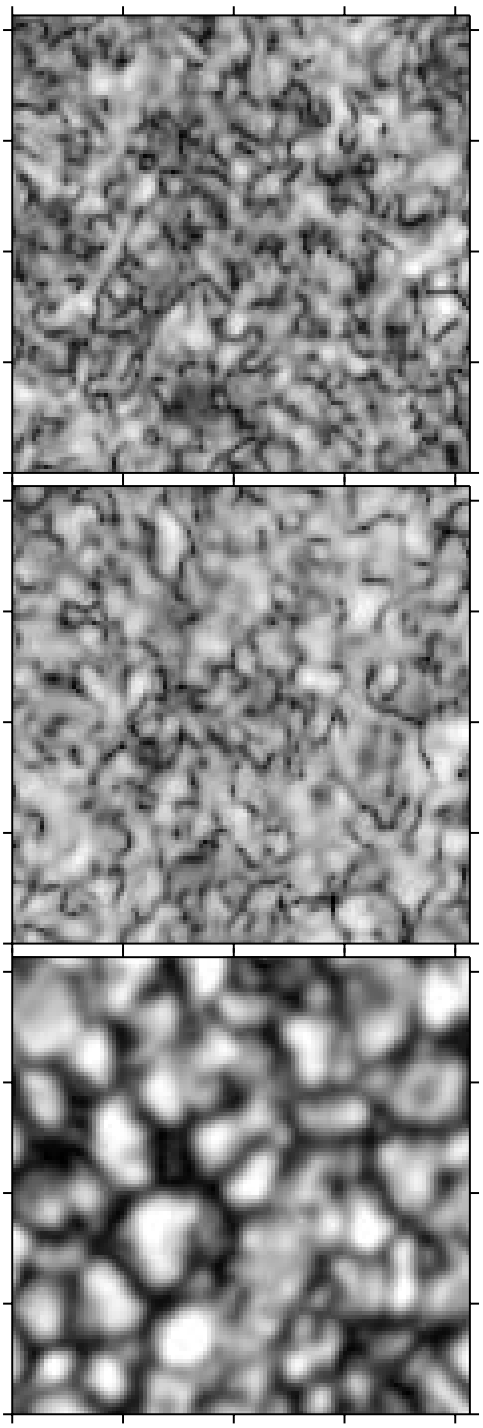

Fig. 4. Enlargements of Fourier amplitude maps from the first 22.4 min data segment (centered at 11:49:00 UT). The greyscale displays $\log A$. Top: Fourier map for 5.5 ± 0.8 mHz (3-min periodicity). Middle: cotemporal and cospatial Fourier map for $f = 3.1 \pm 0.8$ mHz (5-min periodicity). Bottom: cotemporal and cospatial image average. Scale: 10.4×10.4 Mm^2 field (the lower-left corner of the full field shown in Fig. 2). Ticks at 2.5 Mm intervals

pixels of type A are preferentially co-located with pixels of type B and values $C < 1$ imply spatial avoidance.

Due to the large data set used in the present analysis there are always multiple map comparisons per test. Therefore, the rms variances that supply error estimates are based on much better statistics than in Papers I & II. For example, the C value at $\Delta t = 20$ s in Fig. 6 results from averaging over 899 map comparisons, at $\Delta t = 63$ min from 720 map comparisons.

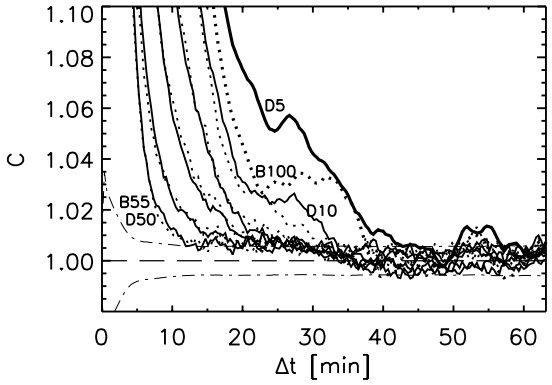

Fig. 5. Brightness evolution. The curves measure time-delay self-correspondence C per equal-area brightness bin, i.e., the amount of alignment of pixels in a given bin between images that were taken Δt min apart. Solid: darker than average brightness. Dotted: brighter than average. The bins are, in pairs from left to right, $45-50\%$ (D50, solid), $50-55\%$ (B55, dotted), $35-40\%$ (solid) and $60-65\%$ (dotted), $25-30\%$ (solid) and $70-75\%$ (dotted), $15-20\%$ (solid) and $80-85\%$ (dotted), $5-10\%$ (D10, solid) and $90-95\%$ (dotted), $0-5\%$ (D5, thick solid) and $95-100\%$ (B100, thick dotted). The 3σ rms range is indicated by the dash-dotted curves above and below the $C = 1$ line

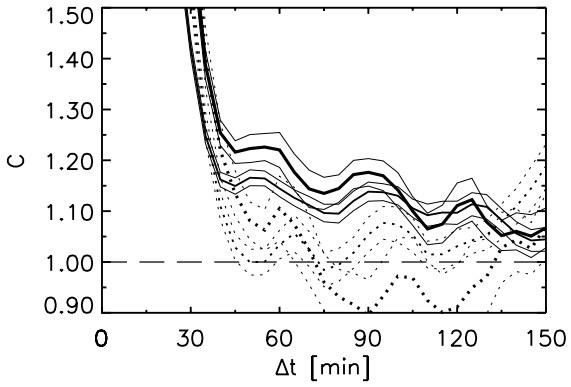

Fig. 6. Persistency evolution. Thick: time delay self-correspondence C for persistency regions containing dark minima (solid) and bright maxima (dashed). Thin: the same, but relaxing the persistency requirement that a pixel is a local extreme. Each curve is plotted together with 1σ variances

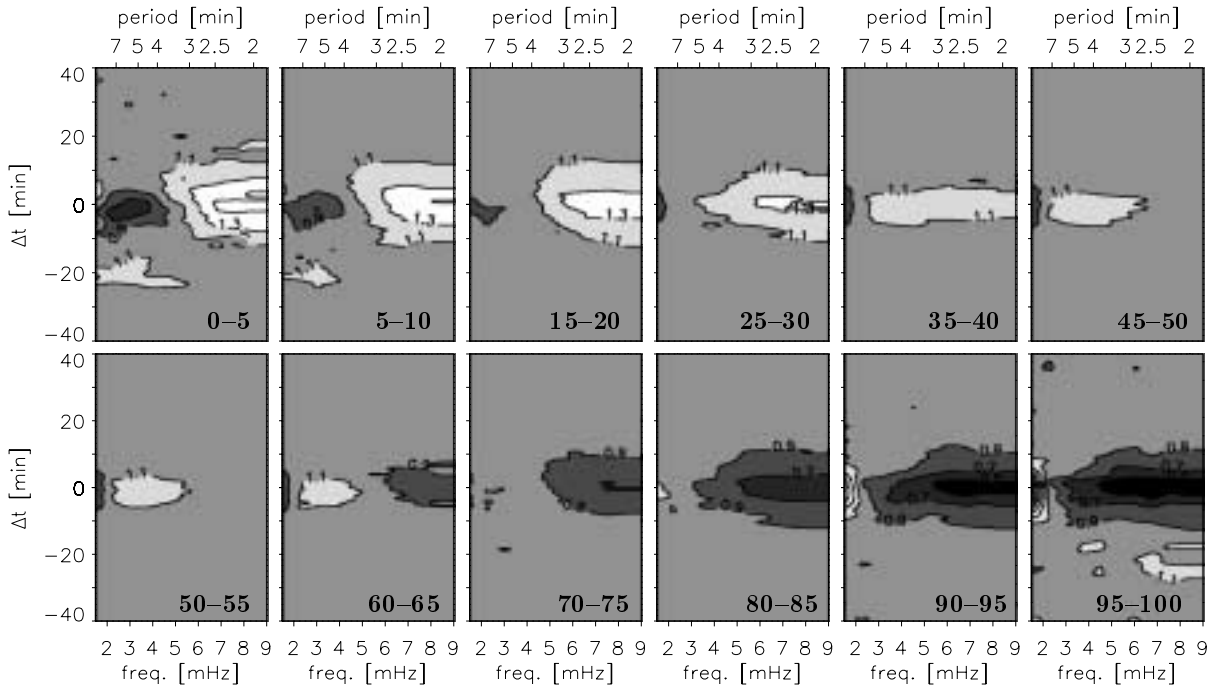

Fig. 7. Time delay charts of the spatial correspondence C between pixels with Fourier amplitudes over twice the average value and pixels in a specific intensity bin, as function of frequency (bottom x axes) or corresponding periodicity (top x axes) and as function of the time lag between the amplitude and brightness measurements (y axes). The intensity bins are specified at the lower right in each panel (the same selection as in Fig. 5), running from the darkest 5% of the pixels in the upper-left panel to the brightest 5% in the lower-right panel. The time lag has $\Delta t > 0$ when brightness is measured after Fourier amplitude. The contour intervals are at $\Delta C = 0.2$ and correspond to 3σ variance. The temporal resolution is $5 - 10$ min. A white peak indicates preferential co-location between higher-than-average Fourier amplitude with the given pixel brightness class, while a dark peak indicates mutual avoidance

3. Results

3.1. Brightness persistence

Figure 5 shows results on the temporal evolution of granular morphology in terms of brightness. The curves measure, per equal-area brightness contour bin, the spatial correspondence between images at different time delays Δt plotted along the horizontal axis. For example, a correspondence value $C = 1.05$ of a particular curve implies that the pixels in the corresponding intensity bin have 1.05 times the 5% random probability to belong again to that bin after Δt min.

All curves drop steeply from high correspondence at small Δt towards $C \approx 1$ at large Δt. The curves for the intermediate bins, generally sampling granular edges, do so the fastest, reaching the 3σ variance above $C = 1$ before $\Delta t = 15$ min. This means that the corresponding granular features loose their identity within this time span: the morphology evolves in such a way that, statistically, no prefered co-location with the original intensity value remains, in agreement with the characteristic granular lifetime of 5–10 min.

However, features that belong to the brightest or the darkest bins display a much longer location memory. Their correspondence values are small but remain significantly above unity out to large Δt. In particular, the curve labeled D5 for the darkest 5% bin, describing minima within dark intergranular lanes, does not reach $C = 1$ to within the 3σ variance until $\Delta t \approx 40$ min. This larger-than-random co-alignment implies that a small but significant fraction of the darkest pixels is preferentially located at sites that were already in the darkest bin much earlier. Curve B100 for the brightest pixels indicates similar persistency, but at lower C out to $\Delta t = 35$ min. The other bins show a gradual progression between these fastest and slowest decays.

Figure 6 is a similar display of time-delay correspondence for the persistency regions defined in Sect. 2.4, split between those containing brightness maxima and those containing brightness minima. Their time-delay self-alignment is here measured over considerably longer times than the 45 min duration over which they are defined. Since there are fewer persistency maps (44) than granulation images (900), there are far fewer map comparisons so that the rms variances are larger than in Fig. 5. The time resolution is also worse since the sampling intervals are 5 min instead of 20 s as in Fig. 5. Nevertheless, Fig. 6 gives significant evidence for yet longer persistency than the steep decay towards $\Delta t \approx 45$ min set by the definition procedure, at

much higher correspondence than in Fig. 5. The persistency regions containing dark minima have $C \approx 1.2$ after one hour, implying that pixels in such regions belong to a dark-minimum persistency region with 20% higher than random probability after this time. Even after two hours, their time-delay correspondence has dropped only to $C \approx 1.1$. This result says that our persistency selection procedure, selecting areas that contain a dark minimum during about 45 min, produces predictive value in finding dark locations over durations that are much longer again. When the initial selection criterion that pixels must be local minima is dropped, the resulting persistency regions also have $C \approx 1.1$ after two hours.

The persistency regions that contain bright maxima rather than dark minima exhibit much less long-term predictive value (dotted curves in Fig. 6). Their time-delay correspondence drops to $C \approx 1.1$ already after one hour and to $C \approx 1.0$ about 15 min later. The drop is even faster when the initial condition requiring local maxima is relaxed. Thus, there is distinct asymmetry in long-term characteristics between the brightest and the darkest locations in the solar granulation. The more so since there are three times as many dark persistency regions as bright persistency regions.

The curves in Fig. 6 display oscillatory behavior with about 35-min periodicity that seems marginally significant with respect to the 1σ variances. This period resembles the width of the initial high-C peak dictated by the persistency definition and seems to portray artificial ringing. Similar modulation was displayed by the self-correspondence curves in Fig. 1 of Paper II, which we attribute to incomplete averaging over mesoscale patterning and mesoscale migration due to the small field size used there. The comparable curves in Fig. 5 are derived from a forty times larger area and indeed do not show such modulation.

3.2. Fourier modulation

Figure 7 displays the degree of time-delay alignment between granular brightness morphology and Fourier amplitude patterning. Each panel shows the spatial correspondence between the pixels belonging to a given 5% brightness bin and the pixels possessing over twice the average Fourier amplitude, as function of Fourier frequency (abscissae, corresponding periodicities along the top) and of time delay Δt. The latter has $\Delta t > 0$ when Fourier maps are compared with brightness maps taken Δt min later. The correspondence values are displayed as greyscale contours in which the values $0.9 < C < 1.1$ make up the grey background, values $C > 1.1$ are bright and values $C < 0.9$ are dark. Each measurement represents a running average over three map comparisons spaced at 20 s temporal separation, subsequently averaged over the three available Fourier maps, and so represents nine comparisons in total. The contour levels are approximately at 3σ spacing. The temporal resolution is set by the Fourier map construction procedure to 5–10 min.

The two extreme panels, upper-left and lower-right, represent new versions of the second and fourth charts in the lower row in Fig. 5 of Paper II. The contours mark the same C intervals, but the variances are three to four times smaller for the new data so that the contour intervals in Fig. 7 portray alignments with higher significance. The present displays are therefore much cleaner. In addition, the larger field size and longer duration of the new data set does away with selective co-alignment due to incomplete mesoscale sampling. The new charts contain fewer correspondence blobs at appreciable time delay than the G and K time-delay charts of Paper II, even though the latter blobs had high statistical significance. Their absence here implies that they were correctly attributed to mesoscale patterning and mesoscale migration in Paper II.

The first panel is for the 0–5% bin describing the darkest intergranular lanes. It shows preferential alignment between pixels with high 2–3 min amplitudes and pixels of extreme darkness, reaching correspondence values as high as $C \approx 1.5$ and confirming the similar peak in the comparable panel of Fig. 5 in Paper II. The large temporal extent of this $C > 1$ blob, about 20 min, illustrates the relatively long persistence of pixels in the the darkest brightness bin shown by Fig. 5.

The brightest pixels (95–100% bin) are compared with high Fourier amplitudes in the last panel at the lower right. Their high-frequency correspondence shows behavior that is opposite to the darkest-pixel excess, in the form of significant below-random cospatiality with regions of high amplitude for $P < 5$ min. In other words, large Fourier amplitudes tend to avoid bright granule centers. We should note that the plotted correspondences measure deviations from spatial averages, so that a blob of high correspondence in one panel of Fig. 7 must necessarily be compensated by a region of low correspondence at the same location in one or more of the other panels (including the missing ones). The bright-granule avoidance by high-frequency modulation therefore represents the same phenomenon as the dark-lane enhancement, since the intermediate panels show a smooth progression between these two extremes.

The high-frequency avoidance blob in the last panel has opposite sign to the high-correspondence peak in the comparable bottom-right panel of Fig. 5 in Paper II. This sign change confirms that the latter peak must be attributed to modulation by seeing jitter which is absent here. In both charts there is a peak of high correspondence at the lowest frequencies. This peak simply represents the time-averaged brightness, showing that bright features are cospatial with themselves. There is no similar self-correspondence peak in the first panel of Fig. 7 because the darkest lanes are dark and produce low zero-frequency amplitude.

At the intermediate frequencies there is a dark blob of avoidance at 4–7 min periodicity in the first panel. It does not necessarily imply that 5-min acoustic waves avoid intergranular lanes, since this blob may also imply compensation for the enhanced 5-min modulation present in the intermediate panels. The latter blobs do not necessarily imply that granular edges emit 5-min waves excessively, because such modulation may also result from morphological evolution. The intermediate bins show the fastest dropoffs in Fig. 5, at about 5 min time scale. This issue is taken up in Sect. 4.

Figure 7 shows only two time-delay blobs of enhanced alignment that seem significant, at $\Delta t = -20$ min in the first and last panels respectively. As noted above, the comparable panels in Fig. 5 of Paper II show much more structure for $\Delta t \neq 0$ due incomplete mesoscale pattern sampling. Such selective co-alignment is suppressed here. The two remaining blobs indicate that, significantly, at the site of dark lanes enhanced low-frequency modulation occurs about twenty minutes later (first panel), whereas enhanced high-frequency modulation occurs preferentially after twenty minutes at bright-granule locations (last panel). Note that these time-delay alignments are only present for the extreme bins, for which Fig. 5 indicates maximum persistence. As in Paper II we suspect that they have to do with mesoscale flow patterning, the topic of our next paper.

Figure 8 presents similar time-delay charts measuring the degree of spatial alignment between the persistency regions and the Fourier modulation patterns. The temporal resolution is only 15–20 min because the persistency maps are derived from long data sequences with much temporal overlap between maps. Features that last less than 15 minutes in these charts are probably not significant.

The two pairs of panels of Fig. 8 are rather similar, implying that the stricter persistency requirement concerning the presence of brightness extrema does not result in larger correspondence values. Furthermore, there is not much difference between the lower pair and the comparable extreme panels of Fig. 7 when the change in temporal resolution is taken into account. Just as in Fig. 7, excess 2–4 min Fourier amplitudes align preferentially with persistency regions containing dark features, whereas high amplitudes counter-correlate with bright-feature persistency at all frequencies. There is no enhancement of this pattern between Fig. 7 and Fig. 8, i.e., when persistency is added as constraint. Thus, dark lanes go with enhanced high-frequency modulation, but selecting persistent dark lanes does not produce additional modulation. This contradicts the expectation for the case that such persistent darkness ("intergranular holes") marks the sites of convective downflow plumes. The latter would be expected to generate excessive sound emission.

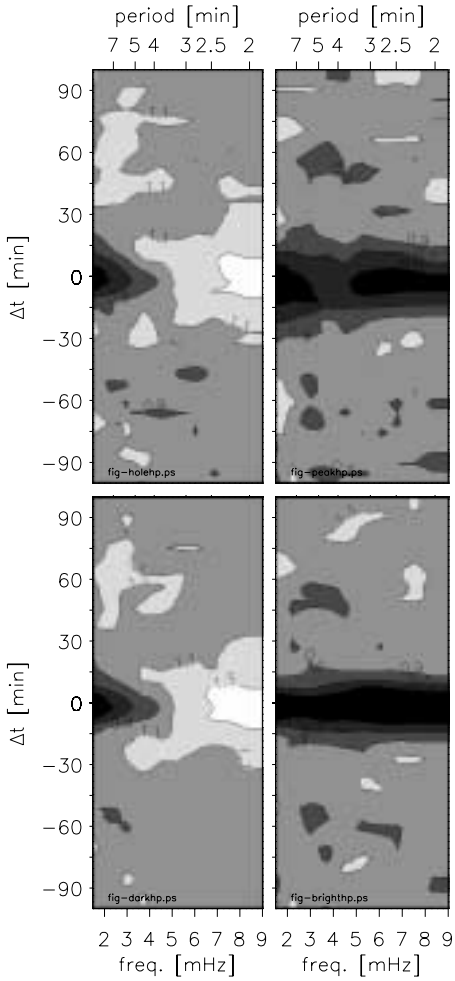

Fig. 8. Time delay charts of the spatial correspondence between pixels with Fourier amplitudes over twice the average value and pixels in a persistency region, respectively for dark persistency regions (upper left) and for bright persistency regions (upper right). The lower panels result when the persistency requirement that a pixel represents a local extreme is dropped. Format and axis labeling as in Fig. 7. The temporal resolution is $15 - 20$ min

4. Discussion

Data quality: 1993 versus 1990. Figures 5 and 7 represent higher-quality updates of Fig. 1 and the G panels of Fig. 5 in Paper II. The quality is much higher due to the better seeing during the 1993 observations, the improved registration techniques (digital rather than analog frame grabbing) and the much larger data set (effectively over 40 times larger because the network was not excluded here). As a result, the high-correspondence peak due to seeing jitter in the bottom-right panel of Fig. 5 in Paper II is now gone, various time-delay correspondences that probably measured incomplete mesoscale sampling have gone, and so have the modulations in the self-correspondence curves in Fig. 1 of Paper II. The charts in Fig. 7 are very clean since the contours are at 3σ rather than 1σ spacing.

Internetwork versus network. The 1990 data set had simultaneous chromospheric coverage which enabled us in Papers I & II to take out the magnetic network by using the Ca II K_{2V} brightness as criterion. The network is not excluded from the purely photospheric 1993 data used here, raising the question to what extent our present results may reflect network behavior alone. In particular, the long-term stationarity indicated for the darkest and the brightest pixels by the slow decay of the pertinent curves in Figs. 5 and 6 may result preferentially from features at the network boundaries. Even if long-lived "intergranular holes" exist within the internetwork regions, they are expected to migrate within a few hours towards the boundaries, driven along by the combination of mesoscale and supergranular flows just as computer-sprinkled corks do (e.g., Title et al. 1989) and is shown by actual solar corks (Brandt et al. 1994). Our persistency finding procedure might miss those internetwork holes when they migrate too fast, while slower migration should yet upset the long-term stationarity indicated for a considerable fraction by Fig. 6. Thus, our results may be dominated by network boundaries rather than by internetwork regions. The same holds, on the same grounds, for the intergranular holes detected by Roudier et al. (1997).

However, we note that the persistency regions do not seem to encompass network bright points (Fig. 3), which might explain long-term stationarity for locally bright pixels, and that the slow self-correspondence decay of the darkest pixels in Fig. 5 is similarly present in the bottom panel of Fig. 2 of Paper II in which the network boundaries were explicitly excluded. The good agreement between the high-frequency modulation enhancements observed at dark lanes in both data sets also suggests that this enhancement represents internetwork or ubiquitous behavior.

Persistence versus recurrence. Figure 5 gives evidence of above-random cospatiality of dark lanes with subsequent dark lanes over durations up to 40 min. The same holds at somewhat smaller correspondence for bright granules. However, it is not clear from this figure whether these features are permanently present over such long periods, or whether they come and go at the same location in recurrent fashion. Such recurrence is not even required at pin-pointed locations because our method expresses correspondence as a statistical deviation from random colocation. Enhanced correspondence may also result from selective recurrence over wider areas than the pixel size. Mesoscale patterning may govern such selective above-random recurrence. Brandt et al. (1991) have shown that regions with divergent mesoscale flows possess more granules than the convergent regions. Therefore, dark lanes may statistically show preferential co-alignment with other dark lanes cropping up earlier in the same mesoscale convergent areas, over the random-draw likelihood normalized by the full area; the same may hold for bright granules. The persistence of such selection should then correspond to the characteristic lifetime of the mesoscale patterns. These indeed evolve and migrate at time scales of an hour and longer (e.g., November et al. 1981; Brandt et al. 1994).

On the other hand, our persistency finding procedure identifies brightness extremes which exist during about 45 min more or less continuously. The additional predictive value that the procedure appears to possess for the darkest pixels, in the form of the high long-term self-correspondence in Fig. 6, indicates that persistency seems an intrinsic property for a significant fraction of the darkest sites in intergranular lanes. This is strikingly less so for the brightest parts of bright granules, for which the curves in Fig. 6 reach $C \approx 1$ soon after the $\Delta t \approx 45$ min definition criterion. This distinct asymmetry between the darkest and brightest locations, also present in the threefold larger occurrence of dark persistency over bright persistency, indicates that the intergranular holes of Roudier et al. (1997) indeed represent a specific phenomenon.

Evolution versus waves. To what extent do our Fourier modulation measurements describe acoustic wave amplitudes? Granular pattern evolution may also produce apparent brightness modulation that is Fourier-decomposed in our Fourier maps at the corresponding periodicity. This will be the case especially at longer periodicities which correspond to characteristic granular lifetimes. The disparity between the 3-min and 5-min amplitude maps and the concurrent granulation morphology shown in the bottom panel of Fig. 4 indicates that granulation morphology is not directly translated into Fourier amplitude morphology. In a coarse sense, the surplus of high-frequency waves at dark intergranular lanes and the wave deficit at bright granules that is quantified in Fig. 7 can also be discerned in Fig. 4, but not at all in one-to-one fashion. The spatial Fourier decompositions in Fig. 8 of Paper I show that larger scales than the granular ones also contribute to the Fourier patterning, as expected for the solar p-mode patterning. We feel that most of the Fourier modulation signal at 5–2 min periodicity represents acoustic waves.

Even if the dark-lane modulation enhancement displayed in the first panel of Fig. 7 represents acoustic wave excess, it does not necessarily imply that intergranular lanes are sites of enhanced acoustic emission. Paper I has suggested subsurface wave diffraction as an alternative or contributing mechanism. Similar anisotropic dispersion by subsurface inhomogeneity is discussed by Zhugzdha (1997b) in the context of p-mode frequency shifts. Zhugzdha (1997a) develops a treatment of acoustic waves in a turbulent atmosphere making use of concepts applied in solid state physics to treat wave propagation in crystal lattices. The presence of enhanced oscillation power with 2–4 min

periodicity at intergranular lanes may be explainable with such a scheme.

As in Papers I & II we have found no indication of the acoustic events with 5-min periodicity at intergranular lanes described by Espagnet (1994), Rimmele et al. (1995) and Espagnet et al. (1996). The only site of some statistical 5-min enhancement in Fig. 7 consists of the intermediate bins describing granular edges, for which the modulation may also be partially due to morphology changes since the corresponding self-correspondence curves in Fig. 5 drop the fastest and over similar time scales. The acoustic events may drown in such changes or not stand out in our statistical averages.

Holes versus plumes. We finally return to the question prompting this paper: do the dark intergranular holes found by Roudier et al. (1997) mark the location of subsurface convective downflow plumes? The answer is inconclusive. Our persistency-finding procedure differs intrinsically from the one of Roudier et al. (1997) by using a different persistency classification scheme and by admitting some lateral motion of the darkest and brightest features. It therefore represents an independent test. The results in Figs. 5–6 indicate that intergranular holes indeed exist as a definite entity possessing abnormally long persistence. The spatial occurrence of our dark-minimum persistency regions amounts to about 8×10^5 on the whole sun at a given moment, about eight times as many as the intergranular holes found by Roudier et al. (1997) which represent a stationary, non-drifting subclass. Only $7 \pm 1.5\%$ of our dark-minimum persistency regions remain stationary over 45 minutes or longer, roughly half the hole occurrence in the data of Roudier et al. (1997). Our results therefore confirm theirs with better statistics due to the wider casting. We have tested whether the stationary subclass behaves differently but found no significant change in co-location properties other than larger noise from the small filling factor.

In addition, Fig. 7 confirms Papers I & II by showing definitely that dark lanes go together with enhanced modulation at 3-min periodicities. However, Fig. 8 does not display the additional excess of locally excited sound that one expects to observe at the sites of strong downflow plumes, and therefore does not supply corroborative evidence for the claim that intergranular holes mark such plumes. Note that even if such enhanced emission is diffracted away from exact co-location at the surface along the lines sketched in Fig. 11 of Paper I, our persistency-finding procedure might still have diagnosed the local sound excess through its perimeter widening.

In conclusion, we haven't found plume noise at intergranular hole sites. This absence does not necessarily upset the plume-driven picture of convection. Our persistency-finding procedure may fail to identify the actual plume sites. It is also possible that the fiercer plumes are relatively scarce. Giant vortices such as the one observed by Brandt et al. (1988) must also be rare since none has been detected in larger-field La Palma and Pic du Midi image sequences since. Vorticity and mesoscale convergence/divergence may provide better plume-finding algorithms than temporal persistency. We will try this in our next paper. In addition, large-area Dopplershift measurements would be useful to enable direct velocity co-location analysis. Finally, it is of interest to subject numerical simulations of the solar convection and of turbulent wave excitation to co-location analyses as performed here.

Acknowledgements. We thank M. Barreto, G. Hosinsky, R. Kever, G. Scharmer, G.W. Simon, and W. Wang for their efficient support in the observations, M. Shand of DEC's Paris office for technical and financial support, W. Mühlmann for help in the initial data analysis, Y.D. Zhugzhda for inspiring discussions, and the referee, Th. Roudier, for constructive comments. This work is based on observations obtained with the Swedish Vacuum Solar Telescope operated by the Royal Swedish Academy of Sciences at the Spanish Observatorio del Roque de los Muchachos of the Instituto de Astrofísica de Canarias. N.M. Hoekzema's research was supported by the Netherlands Foundation for Research in Astronomy with financial aid from the Netherlands Organization for Scientific Research and by the Kiepenheuer-Institut für Sonnenphysik, which he thanks for hospitality.

References

Berger T. E., Title A. M., 1996, ApJ 463, 365
Berger T. E., Schrijver C. J., Shine R. A., et al., 1995, ApJ 454, 531
Brandt P. N., Scharmer G. B., Ferguson S. H., et al., 1988, Nat 335, 238
Brandt P. N., Ferguson S., Scharmer G. B., et al., 1991, A&A 241, 219
Brandt P. N., Rutten R. J., Shine R. A., Trujillo Bueno J., 1994, in R. J. Rutten, C. J. Schrijver (eds.), Solar Surface Magnetism, NATO ASI Series C 433, Kluwer, Dordrecht, p. 251
Brown T. M., 1991, ApJ 371, 396
Brown T. M., Bogdan T. J., Lites B. W., Thomas J. H., 1992, ApJ 394, L65
Brummell N. H., Hurlburt N. E., Toomre J., 1996, ApJ 473, 494
Cattaneo F., Brummell N. H., Toomre J., Malagoli A., Hurlburt N. E., 1991, ApJ 370, 282
Espagnet O., 1994, La granulation solaire: origine, pénétration dans la photosphère et interactions avec les oscillations de 5 minutes, Thesis Université Paul Sabatier, Toulouse
Espagnet O., Muller R., Roudier T., et al., 1996, A&A 313, 297
Goode P. R., Gough D., Kosovichev A. G., 1992, ApJ 387, 707
Hirzberger J., Vazquez M., Bonet J. A., Hanslmeier A., Sobotka M., 1997, ApJ 480, 406
Hoekzema N. M., Brandt P. N., Rutten R. J., 1998a, A&A submitted
Hoekzema N. M., Rutten R. J., Brandt P. N., Shine R. A., 1998b, A&A 329, 276

Muller R., Roudier T., 1992, Solar Phys. 141, 27
Muller R., Hulot J. C., Roudier T., 1989, Solar Phys. 119, 229
November L. J., Toomre J., Gebbie K. B., Simon G. W., 1981, ApJ 245, L123
Rast M. P., 1995, ApJ 443, 863
Restaino S. R., Stebbins R. T., Goode P. R., 1993, ApJ 408, L57
Rieutord M., Zahn J.-P., 1997, ApJ 474, 760
Rimmele T. R., Goode P. R., Harold E., Stebbins R. T., 1995, ApJ 444, L119
Roudier T., Espagnet O., Muller R., Vigneau J., 1994, A&A 287, 982
Roudier T., Malherbe J. M., November L., et al., 1997, A&A 320, 605
Scharmer G. B., 1989, in R. J. Rutten, G. Severino (eds.), Solar and Stellar Granulation, NATO ASI Series C 263, Kluwer, Dordrecht, p. 161
Scharmer G., Lofdahl M., 1991, Advances in Space Research 11, 129
Scharmer G., Brown D., Petterson L., Rehn J., 1985, Appl. Opt. 24, 2558
Shine R. A., Title A. M., Tarbell T. D., et al., 1994, ApJ 430, 413
Simon G. W., Brandt P. N., November L. J., Scharmer G. B., Shine R. A., 1994, in R. J. Rutten, C. J. Schrijver (eds.), Solar Surface Magnetism, NATO ASI Series C 433, Kluwer, Dordrecht, p. 261
Simon G. W., Title A. M., Weiss N. O., 1991, ApJ 375, 775
Simon G. W., Title A. M., Weiss N. O., 1995, ApJ 442, 886
Sobotka M., Bonet J. A., Vazquez M., 1993, ApJ 415, 832
Spruit H. C., Schüssler M., Solanki S. K., 1991, in A. N. Cox, W. C. Livingston, S. Matthews (eds.), Solar interior and atmosphere, Univ. Arizona Press, Tucson, p. 890
Stein R. F., Nordlund Å., 1989, ApJ 342, L95
Title A. M., Tarbell T. D., Topka K. P., Ferguson S. H., Shine R. A., the SOUP Team, 1989, ApJ 336, 475
Zhugzdha Y. D., 1997a, A&A submitted
Zhugzdha Y. D., 1997b, in F. P. Pijpers, J. Christensen-Dalsgaard, C. S. Rosenthal (eds.), Solar Convection and Oscillation and their Relationship, Procs. SCORe96, Kluwer, Dordrecht, in press